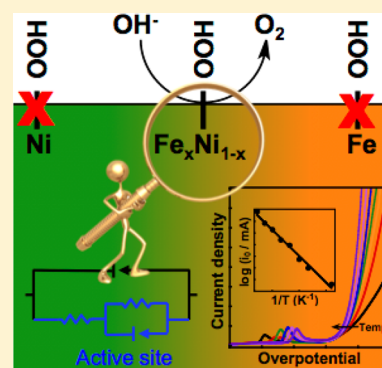


## Electrochemical Study of the Energetics of the Oxygen Evolution Reaction at Nickel Iron (Oxy)Hydroxide Catalysts

John R. Swierk,<sup>\*,†</sup> Shannon Klaus,<sup>‡,§</sup> Lena Trotochaud,<sup>†</sup> Alexis T. Bell,<sup>†,§</sup> and T. Don Tilley<sup>\*,†,§</sup><sup>†</sup>Joint Center for Artificial Photosynthesis, Materials Science Division, Lawrence Berkeley National Laboratory, Berkeley, California 94720, United States<sup>‡</sup>Department of Chemical and Biomolecular Engineering and <sup>§</sup>Department of Chemistry, University of California—Berkeley, Berkeley, California 94720, United States

## S Supporting Information

**ABSTRACT:** Iron-doped nickel (oxy)hydroxide catalysts ( $\text{Fe}_x\text{Ni}_{1-x}\text{OOH}$ ) exhibit high electrocatalytic behavior for the oxygen evolution reaction in base. Recent findings suggest that the incorporation of  $\text{Fe}^{3+}$  into a  $\text{NiOOH}$  lattice leads to nearly optimal adsorption energies for OER intermediates on active Fe sites. Utilizing electrochemical impedance spectroscopy and activation energy measurements, we find that pure  $\text{NiOOH}$  and  $\text{FeOOH}$  catalysts exhibit exceedingly high Faradaic resistances and activation energies 40–50  $\text{kJ/mol}^{-1}$  higher than those of the most active  $\text{Fe}_x\text{Ni}_{1-x}\text{OOH}$  catalysts. Furthermore, the most active  $\text{Fe}_x\text{Ni}_{1-x}\text{OOH}$  catalysts in this study exhibit activation energies that approach those previously reported for  $\text{IrO}_2$  OER catalysts.



Currently, 55 million metric tons of hydrogen are produced globally each year, 95% of which is produced from nonrenewable sources.<sup>1</sup> At the same time, the demand for renewable sources of energy is increasing: over 65% of federal energy subsidies outside the electricity sector were devoted to renewable fuel generation in 2013.<sup>2</sup> For many renewable fuel systems, hydrogen gas is a necessary component, making the renewable production of hydrogen gas an urgent scientific challenge.<sup>3</sup> Direct electrolysis of water to form molecular hydrogen and oxygen currently represents the most promising route to renewable hydrogen production. Unfortunately, the slow kinetics of the oxygen evolution reaction ( $\text{OER}$ ,  $4\text{OH}^- \rightarrow 2\text{H}_2\text{O} + \text{O}_2 + 4\text{e}^-$  in base and  $2\text{H}_2\text{O} \rightarrow 4\text{H}^+ + \text{O}_2 + 4\text{e}^-$  in acid) requires large reaction overpotentials, fundamentally limiting the overall efficiency of this process.

Though much of the early work on OER catalysts focused on the use of noble metals and their oxides ( $\text{IrO}_2$ ,  $\text{RuO}_2$ ,  $\text{Pt}$ ,  $\text{Rh}$ , etc.)<sup>4–11</sup> because of their high electrocatalytic activity and stability, recent work has emphasized the development of first-row transition-metal catalysts as more economical options.<sup>12</sup> Of the proposed catalysts, iron-doped nickel oxide/(oxy)hydroxide catalysts show the most promise,<sup>13–25</sup> by some metrics matching or exceeding the performance of  $\text{IrO}_2$ , which is generally accepted as one of the best OER catalysts.<sup>19,26</sup>

The mechanism underlying the high catalytic activity in iron-doped nickel catalysts has generated much interest. Initial focus centered on the role of nickel in the catalyst. A consensus emerged that a  $\text{NiOOH}$ -type structure was responsible for the OER activity, with aging in base promoting a conversion from a  $\gamma$ - $\text{NiOOH}$ -like phase to a more active  $\beta$ - $\text{NiOOH}$

phase.<sup>14,15,18,27,28</sup> Iron incorporation was thought to primarily tune the redox properties of the active nickel sites while inducing some structural disorder. Trotochaud et al. later revealed that the source of catalytic activity on pure nickel electrodes was due to incidental iron contamination from trace iron in the electrolyte.<sup>29</sup> In iron-free electrolyte, they showed that  $\text{NiOOH}$  is in fact an exceedingly poor OER catalyst; this finding suggested that, in iron-doped nickel (oxy)hydroxide catalysts, Fe played a more critical role in OER catalysis than previously appreciated. Recently, Friebe et al. utilized a combination of operando X-ray absorption spectroscopy and density-functional theory calculations to demonstrate that the increased OER activity in iron-doped nickel oxide catalysts is likely due to  $\text{Fe}^{3+}$  incorporated into a  $\gamma$ - $\text{NiOOH}$ -like phase.<sup>30</sup> Upon oxidation to OER potentials, there is a 7% contraction of the Fe–O bond length in  $\text{Fe}_x\text{Ni}_{1-x}\text{OOH}$  relative to that in  $\gamma$ - $\text{FeOOH}$ . Calculations suggest that this bond length contraction enables more optimal adsorption energies of OER intermediates ( $-\text{OH}$ ,  $-\text{O}$ , and  $-\text{OOH}$ ) over these Fe sites, which is the cause of increased OER activity of  $\text{Fe}_x\text{Ni}_{1-x}\text{OOH}$  materials.

In this study, we experimentally probe the energetics of OER catalysis on electrodeposited iron-doped nickel (oxy)hydroxide catalysts ( $\text{Fe}_x\text{Ni}_{1-x}\text{OOH}$ ). Utilizing a combination of impedance spectroscopy and activation energy measurements, we demonstrate that OER catalysis is energetically more favorable on  $\text{Fe}_x\text{Ni}_{1-x}\text{OOH}$  catalysts than on pure  $\text{NiOOH}$  or  $\text{FeOOH}$ .

Received: June 19, 2015

Revised: July 26, 2015

Published: July 28, 2015



The measured Faradaic resistances for  $\text{Fe}_x\text{Ni}_{1-x}\text{OOH}$  are typically 1 to 2 orders of magnitude smaller than on the monometallic catalysts. Compared to  $\text{NiOOH}$ , there is a 3-fold decrease in the OER activation energy for the most active  $\text{Fe}_x\text{Ni}_{1-x}\text{OOH}$  catalysts. We also show that the OER activation energy for highly active  $\text{Fe}_x\text{Ni}_{1-x}\text{OOH}$  catalysts is similar to the measured activation energies of  $\text{IrO}_2$  OER catalysts. Finally, we present the first impedance measurements, to our knowledge, of an Fe-free  $\text{NiOOH}$  electrode at oxygen evolution potentials.

## 2. EXPERIMENTAL SECTION

**2.1. Electrocatalyst Preparation.** Electrocatalytic films containing Ni and/or Fe were deposited onto 5 mm gold disk electrodes sheathed by a Teflon cup. Prior to electrodeposition, the gold electrodes were mechanically polished with 1 and 0.05  $\mu\text{m}$  alumina slurries, with 10 min of sonication in high-purity water after each polishing step. The gold electrodes were then electrochemically polished by cycling from  $-1$  to  $0.7$  V vs  $\text{Hg}/\text{HgO}$  in Fe-free 1 M KOH for 25 cycles at a scan rate of  $100 \text{ mV s}^{-1}$ .

Films were deposited via the method of Louie and Bell<sup>18</sup> at a constant current density of  $-50 \text{ mA cm}^{-2}$  for 113 s without stirring. The deposition solution was prepared by dissolving nickel sulfate hexahydrate (99.99%) and/or iron sulfate heptahydrate (99%) in  $18.2 \text{ M}\Omega \text{ cm}$  nanopure water. Before the metal salts were added, the solution was sparged with argon for at least 45 min and sparged for an additional 15 min after the addition of the metal salts. The potential during film deposition was measured relative to a  $\text{Ag}/\text{AgCl}$  (sat. KCl) reference electrode ( $0.197 \text{ V}$  vs NHE, BAS Inc.).

The film compositions were determined from XPS measurements. A Mg  $K\alpha$  nonmonochromated X-ray source was used to avoid the overlap of the Fe 2p region with Ni Auger features (which occurs with an Al source).

**2.2. Electrochemical Characterization.** All experiments were conducted in Fe-free 1 M KOH<sup>26</sup> under air using a Biologic SP300 potentiostat. Potentials were referenced against a  $\text{Hg}/\text{HgO}$  (1 M KOH) electrode ( $0.140 \text{ V}$  vs NHE, CH Instruments) with a piece of platinum mesh used as the counter electrode. A PTFE cup was used as the cell instead of glass to prevent etching, which occurs in alkaline electrolytes. The double-layer capacitance for each film was measured in a static solution, whereas all other measurements were made at a constant rotation of 1600 rpm to minimize mass transport effects. The stability of the catalyst films was characterized by linear sweep voltammetry every 2 h over the course of 2 days. In the interim between scans, the samples were allowed to stir at open circuit.

Prior to the impedance measurements, the electrodes were held at a constant overpotential for 15 min to ensure a stable current. A 10 mV ac perturbation voltage was applied on top of a given dc overpotential, and the frequency was scanned from 10 MHz to 100 mHz. At each frequency, the length of two periods occurred before taking the average of two measurements. A total of three to four unique samples were measured for each given film composition.

For temperature-dependent measurements, the PTFE cup was sealed with a custom-made lid and then suspended in a thermostated water bath. The electrodes were passed through holes in the lid slightly larger than the electrodes to minimize evaporative losses. The value of the exchange current density,  $\log(j_0/\text{mA cm}^{-2})$ , at each given temperature was determined from the equation of the Tafel slope, with the potential (in

millivolts) of the reference electrode corrected for temperature (in Kelvin) using<sup>31</sup>

$$E_{\text{Hg}}^{\circ}|\text{HgO}|\text{OH}^- = 109.27 + 1.0042T - 0.0034805T^2$$

## 3. RESULTS AND DISCUSSION

**3.1. Electrocatalyst Characterization.** Previously, Louie and Bell determined that the iron concentration in  $\text{Fe}_x\text{Ni}_{1-x}\text{OOH}$  catalysts is not linearly proportional to the concentration of iron in the deposition solution.<sup>18</sup> At solution concentrations above 50% iron, the iron apparently under-deposits, whereas iron overdeposits within the catalytic film at iron solution concentrations of less than 50%. We observed an identical deposition behavior and found film compositions (determined by XPS) within 1 to 2% of the values reported by Louie and Bell for identical iron and nickel solution concentrations (Figure S1). For the 100% Ni films, no iron contamination was detected by XPS. At high nickel and iron concentrations, small peaks indicating the presence of a metallic phase were observed in the as-deposited films. Under OER conditions, however, the metallic phase is converted to the (oxy)hydroxide phase.<sup>18</sup>

The cyclic voltammograms (Figure 1) of the 100% Ni films exhibited the expected  $\text{Ni}(\text{OH})_2/\text{NiOOH}$  redox peaks centered

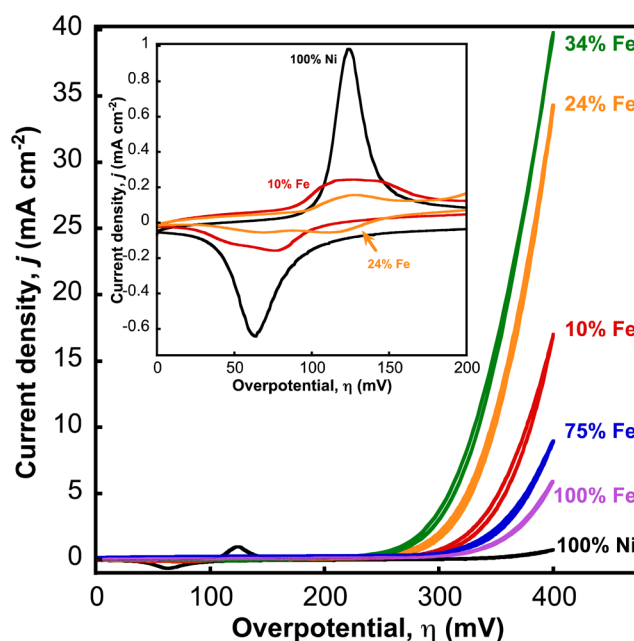


**Figure 1.** Cyclic voltammograms of electrocatalyst films with various iron compositions in 1 M KOH ( $E_{\text{H}_2\text{O}/\text{O}_2} = 310 \text{ mV}$  vs  $\text{Hg}/\text{HgO}$  at  $21^\circ\text{C}$ , scan rate =  $10 \text{ mV s}^{-1}$ ).

at approximately 400 mV vs  $\text{Hg}/\text{HgO}$ . These peaks can also be observed in the 10 and 24% Fe films, though they are smaller for these films. For the 100% Ni film, integration of  $\alpha\text{-Ni}(\text{OH})_2/\gamma\text{-NiOOH}$  peaks gave an effective film thickness of  $\sim 7 \text{ nm}$ , assuming  $1 \text{ e}^-$  per Ni<sup>26</sup> and a density<sup>32</sup> of  $1.25 \text{ g cm}^{-3}$ . Accounting for the 10-fold difference in deposition time, the film thickness is in excellent agreement with the thicknesses measured by Louie and Bell ( $\sim 70 \text{ nm}$ ).<sup>18</sup> On the basis of this agreement, we assume that all films in this study are approximately  $\sim 7 \text{ nm}$  thick. We determined the double-layer

capacitance measured in a 0.1 V potential window centered around the open-circuit potential (Figure S2).<sup>33</sup>

Figure 1 presents representative cyclic voltammograms for films with various Fe compositions. As expected, in Fe-free 1 M KOH, the pure NiOOH catalyst showed little activity at overpotentials of less than 400 mV, and more than 533 mV of overpotential (Figure 2) is needed to achieve a 10 mA cm<sup>-2</sup>

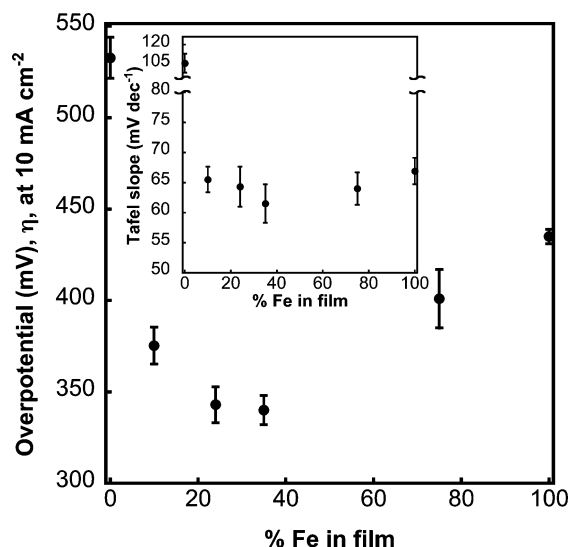


**Figure 2.** Overpotential required for a current density of 10 mA cm<sup>-2</sup> in 1 M KOH as a function of Fe concentration ( $E_{\text{H}_2\text{O}/\text{O}_2} = 310$  mV vs Hg/HgO at 21 °C). Inset: Tafel slope as a function of Fe concentration in the film.

geometric current density. Klaus et al. reported a similar overpotential for NiOOH in Fe-free 1 M KOH.<sup>29</sup> With increasing iron concentration, the OER activity increased, reaching an apparent maximum at ~35% Fe before decreasing at higher iron concentrations. The maximum solubility of iron in NiOOH is estimated to be between 11 and 25% before iron begins to segregate into less active FeOOH domains.<sup>29,30</sup>

Contrary to the frequently observed Tafel slope behavior of ca. 40 mV dec<sup>-1</sup>,<sup>18,25,29</sup> we observed typical Tafel slopes of ca. 60 mV dec<sup>-1</sup> (Figure 2, inset; Figure S3). Generally, a Tafel slope of ca. 40 mV dec<sup>-1</sup> is ascribed to a rate-determining step involving the second electron transfer, whereas a slope of ca. 60 mV dec<sup>-1</sup> is usually diagnostic of a rate-determining step involving a chemical transformation following the first electron transfer.<sup>34,35</sup> Doyle and Lyons have extensively investigated the Tafel behavior of hydrous iron oxide electrodes in base and suggest that a Tafel slope of ca. 60 mV dec<sup>-1</sup> is indicative of a dehydrated film. These authors demonstrated that aging an electrode in base can convert a film with a Tafel slope of ca. 40 mV dec<sup>-1</sup> into a film displaying a slope of ca. 60 mV dec<sup>-1</sup>. In this study, the films were dried under a stream of N<sub>2</sub> after deposition, which may contribute to film dehydration. Also, the Tafel slopes were measured after five cycles between  $\eta = 0$  and 400 mV in 1 M Fe-free KOH to ensure the full conversion of any metallic species and achieve a stable  $j$ - $V$  curve. Tafel slopes determined from the first cycle were typically 4 to 5 mV dec<sup>-1</sup> lower, suggesting some film dehydration with cycling. Louie and Bell<sup>18</sup> commented on the need to cycle NiFe films 5–10 times before a stable OER current is obtained, which may also be indicative of a dehydration process upon initial immersion in KOH. For comparison, freshly prepared 35% Fe films that were

kept wet exhibited a Tafel slope of  $48 \pm 1$  mV dec<sup>-1</sup>, which changed to  $74 \pm 2$  mV dec<sup>-1</sup> after stirring in Fe-free 1 M KOH for 2 days. Although Fe<sub>x</sub>Ni<sub>1-x</sub>OOH catalysts exhibit stable activity over at least 2 h,<sup>18</sup> these results suggest that longer-term studies are needed to adequately understand the performance of Fe<sub>x</sub>Ni<sub>1-x</sub>OOH in photoelectrochemical systems, which cycle between periods of activity (daytime) and inactivity (night-time).

**3.2. Electrochemical Impedance.** As an analytical technique that can be applied to a working catalyst, electrochemical impedance spectroscopy (EIS) offers an opportunity to explore the underlying controlling factors of catalyst activity as a function of overpotential and composition. In an EIS measurement, a small ac perturbation voltage ( $\leq 10$  mV) is superimposed on a dc voltage. The current response is measured over a range of frequencies, with different electrochemical processes resolved as a function of frequency. Merrill and Dougherty<sup>36</sup> and Huang et al.<sup>22</sup> briefly explored the impedance of a single nickel–iron composition but did not attempt to fit the data to an equivalent circuit. Furthermore, whereas previous studies have considered the EIS of Ni OER catalysts,<sup>37–44</sup> those studies are likely to suffer from Fe contamination.

Lyons and co-workers have extensively considered the EIS of hydrated metal oxide OER catalysts,<sup>34,38,45,46</sup> which was heavily informed by the earlier works of Cahan and Chen<sup>47,48</sup> as well as Harrington and Conway.<sup>49</sup> Figure 3 shows the equivalent

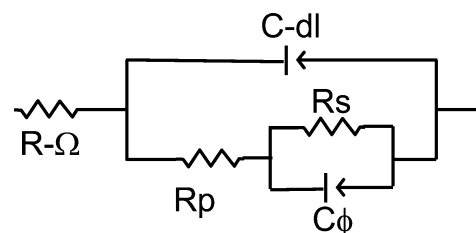


**Figure 3.** Equivalent circuit for OER catalysts without an RC loop related to film resistance.

circuit proposed to model the OER. Generally,  $R-\Omega$  describes the uncompensated for solution resistance, and  $C\text{-dl}$  describes the double-layer capacitance. The Faradaic OER is treated by the three circuit components,  $R_s$ ,  $R_p$ , and  $C\phi$ , which do not describe single charge-transfer processes; instead, each component handles multiple steps within the overall reaction.<sup>38,49</sup>  $R_p$ , the polarization resistance, is related to the overall rate of the OER and incorporates the charge-transfer resistances of the various steps within the OER up to and including the rate-determining step. In a general way,  $R_s$  is related to the ease with which one or more surface intermediates are formed. Together the two give the Faradaic resistance of the catalyst, which is simply defined as  $R_{\text{far}} = R_s + R_p$ . Together with  $C\phi$ , the  $R_sC\phi$  loop models the relaxation of charge associated with the formation of surface intermediates. Broadly,  $C\phi$  describes the change in charged surface species as the OER proceeds. In many instances, an additional RC loop that models the film resistance and capacitance is included in series with the circuit shown in Figure 3. To allow for a uniform application of the circuit in Figure 3, a measurement window (10 kHz to 0.1 Hz) was chosen that would exclude the loop related to film resistance and capacitance. On the basis of the resistivities of Ni(OH)<sub>2</sub>/NiOOH ( $10^1$ – $10^6$  Ω cm<sup>-1</sup>)<sup>50–53</sup> and



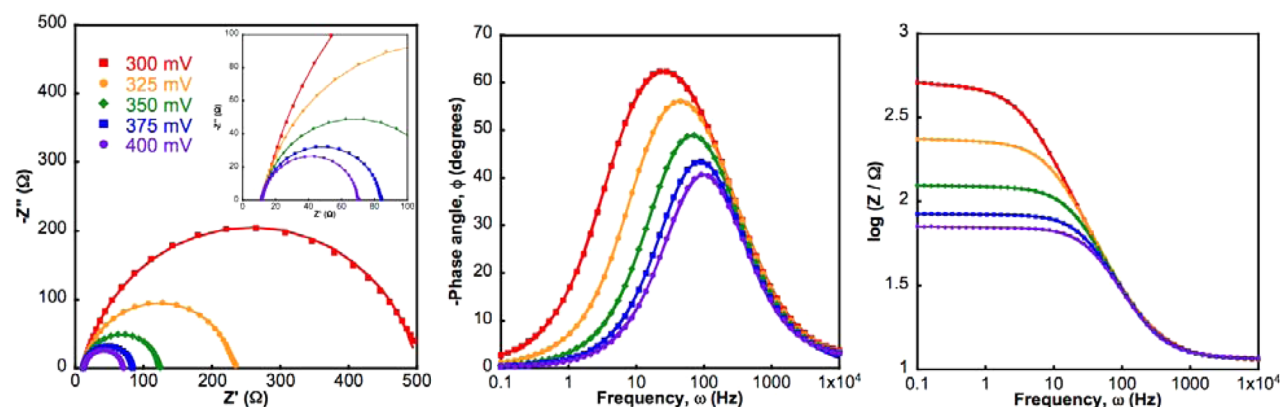


Figure 4. Representative Nyquist, phase, and Bode plots of a 25% Fe catalyst.

FeOOH ( $10^5$ – $10^7 \Omega \text{ cm}^{-1}$ ),<sup>35,54,55</sup> the film thickness (7 nm), the film area ( $0.2 \text{ cm}^2$ ), and a reasonable estimate of the film capacitance ( $0.1$ – $10 \mu\text{F cm}^{-2}$ ),<sup>45,55</sup> we estimate that the RC time constant of this loop should lie outside the measurement window and contribute little to the 10 kHz to 0.1 Hz range, though we cannot exclude some contribution to  $R$ – $\Omega$  from this loop. As we show below, this assumption is valid, as no feature in the Nyquist or phase plot is observed that can be assigned to an RC component related to the film resistance and capacitance.

Representative Nyquist, phase, and Bode plots for each catalyst composition are shown in Figure 4 and Figures S5–S9. All of the Nyquist plots showed a flattening of the semicircle, indicative of a dispersive capacitance. To address this dispersion, constant phase elements (CPEs) were used in modeling C-dl and  $C\phi$ . The CPE is defined as

$$\frac{1}{Z_{\text{CPE}}} = Q(i\omega)^\alpha$$

where  $Z_{\text{CPE}}$  is the impedance of the CPE. If  $\alpha = 1$ , then the CPE describes an ideal capacitor with  $Q = C$ , and when  $\alpha = 0$ , the CPE describes an ideal resistor with  $Q = R$ .<sup>56</sup> Although the precise physical interpretation of the CPE is unclear,  $\alpha$  is generally taken as an indicator of the homogeneity and uniformity of the electrode.<sup>45</sup>

In the phase plots, we generally observed a single peak between 10 and 1000 Hz, which appears to correlate with the characteristic frequency associated with the RC time constant of the  $R_sC\phi$  loop. This suggests that the catalysis of  $\text{Fe}_x\text{Ni}_{1-x}\text{OOH}$  in these films is dominated by the formation of chemical intermediates and not electron-transfer steps, which is consistent with the observed Tafel slopes of ca.  $60 \text{ mV dec}^{-1}$ . We also observed only a single step in the Bode plots, again demonstrating that  $R_sC\phi$  is the dominant process. Typically, the optimum fit values for  $R_s$  were significantly larger than for  $R_p$ , with differences greater than 1 order of magnitude not uncommon (Table S1–S5).

Figure 5 shows the variation of  $R_s$  both with composition and overpotential. With increasing overpotential, the magnitude of  $R_s$  decreased for all compositions, which is to be expected for a Faradaic reaction. The 0 and 100% Fe catalysts exhibited significantly higher  $R_s$  values when compared to the mixed compositions, with a nearly 2 order of magnitude difference between the  $R_s$  values of 0% Fe and 35% Fe films, for example. This offers insight into the significant difference in activity observed. On a monometallic (oxy)hydroxide surface, the high

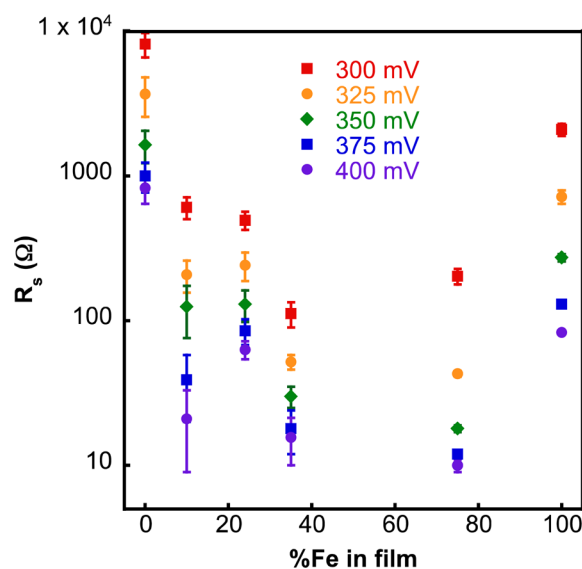
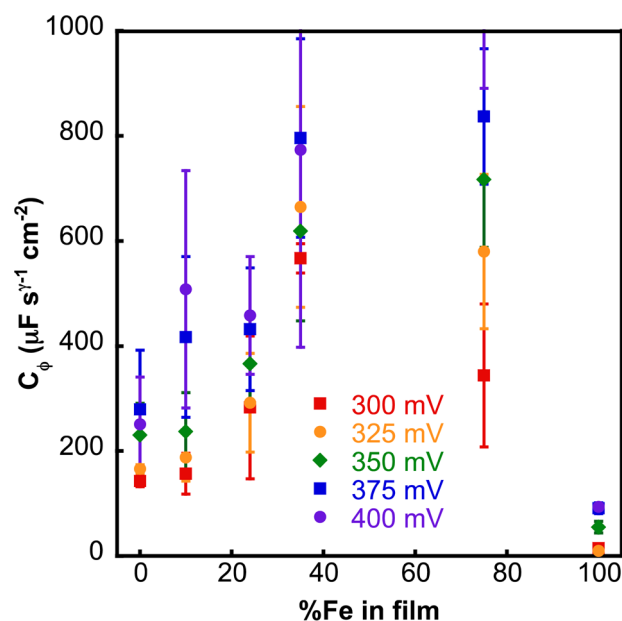


Figure 5. Optimum fitting values for  $R_s$  as a function of catalyst composition and overpotential.

values of  $R_s$  indicate that the stabilization of chemical intermediates is difficult. For an Fe site incorporated into a NiOOH lattice, the stabilization of chemical intermediates becomes markedly easier, as demonstrated by the significant decrease in  $R_s$  at 10–75% Fe. The trends we observed in  $R_s$  can be well described computationally. DFT + U calculations suggest that on FeOOH, OER intermediates are too strongly bound for effective catalysis, but they are too weakly bound on NiOOH. When an Fe site is surrounded by Ni next-nearest neighbors, the affinity for binding OER intermediates decreases and tends toward an optimal value.<sup>30</sup> Interestingly, at high overpotentials the bimetallic catalysts exhibited similar  $R_s$  values despite differences in catalytic activity. This suggests that  $R_s$  is not the sole controlling factor for OER activity.

In the equivalent circuit for OER catalysis,  $R_s$  is in parallel with a capacitance ( $C\phi$ ), which aids in modeling charge relaxation related to the production of surface intermediates. In Figure 6, we show that  $C\phi$  reached an apparent maximum between 35 and 75% Fe. Of particular note, the values of  $C\phi$  for 100% Fe are significantly lower than any other catalyst composition. This may be related to the low conductivity of FeOOH,<sup>35,54,55</sup> making it unable to efficiently allow for charge relaxation.



**Figure 6.** Optimum fitting values for  $C\phi$  as a function of catalyst composition and overpotential.

It is interesting that the  $R_s$  and  $C\phi$  values for the 75% Fe catalyst suggest that this composition should be a highly active OER catalyst, although Figure 2 shows that it is notably less active than 25 or 35% Fe. We can suggest a possible explanation for this discrepancy by considering the physical structure of the catalyst. From XAS measurements, Friebe et al.<sup>30</sup> suggest that a 75% Fe catalyst film is composed of islands of FeOOH surrounded by veins of Fe-saturated NiOOH. It is most likely that these veins of Fe-saturated NiOOH contribute to the OER catalysis; as the Fe sites in these veins are chemically identical to those in other Fe-doped compositions, it is reasonable that the energetics should be similar. However, the current passed at a given overpotential depends on more than just the energetics of the catalytically active site. The total number of accessible sites will also control the current observed at a given overpotential. Figure S2 shows that the open-circuit double-layer capacitance, which correlates with the accessible surface area, is significantly less for iron-rich compositions than for nickel-rich compositions. Furthermore, as the overpotential increased, we saw a decrease in the double-layer capacitance (Figure S10), which is commonly observed and ascribed to the formation of bubbles blocking active sites.<sup>46</sup> Thus, although the active site energetics on a 75% Fe catalyst are similar to those of lower Fe content catalysts, the 75% contains significantly fewer accessible active sites. As a final note, we saw a consistent trend in C-dl with potential, suggesting that we are in fact measuring an authentic capacitance associated with the catalytic film and not the underlying substrate, though we cannot exclude that some sites are inaccessible due to poor film conductivity.

Interestingly, the electrodeposited FeOOH films in this study exhibit a significant enhancement relative to hydrous iron oxide films prepared by cycling metallic Fe in base, most heavily studied by Lyons and co-workers.<sup>45,46</sup> For example, at an overpotential of 350 mV, the  $R_s$  value for the FeOOH films in our study is  $273 \pm 16 \Omega$ , whereas Doyle and Lyons<sup>45</sup> report values of 13 420 and 32 080  $\Omega$ , depending on the method of preparation. There is also a roughly 1 order of magnitude difference in the  $R_p$  values between the Fe films in our study

and those reported by Doyle and Lyons. The large differences in  $R_s$  and  $R_p$  are manifest in a nearly 100 mV increase in the overpotential needed to reach  $10 \text{ mA cm}^{-2}$  for hydrous iron oxide films. Interestingly, at the same overpotential there is good agreement between the two studies in the value of  $C\phi$ ,  $55 \pm 11 \mu\text{F cm}^{-2}$  in our study as compared to 13.4 and  $41.6 \mu\text{F cm}^{-2}$ , and the double-layer capacitances,  $75 \pm 13$  versus ca.  $44 \mu\text{F cm}^{-2}$ . Although a direct comparison is difficult because of a probable difference in film thickness, the similarity in  $C\phi$  and C-dl suggests that even for two nominally similar catalysts the OER mechanism and activity, reflected in  $R_p$  and  $R_s$ , strongly depend on the local structure around the active site. The hydrous iron oxide films are considered to be composed of a compact inner layer and an open, polymeric phase that has a repeating unit of  $[\text{Fe}_2\text{O}_3(\text{OH})_3(\text{OH}_2)_3]^{3-}$ , with counterions maintaining charge neutrality.<sup>34</sup> By contrast,  $\gamma$ -FeOOH is formally neutral and relatively compact, with slabs of octahedral Fe bound together through shared oxygen atoms. On a  $\gamma$ -FeOOH-like structure, the lowest-energy mechanism is calculated to go through a bridged oxygen atom intermediate involving two adjacent Fe sites on the face of the slabs,<sup>30</sup> whereas in hydrous iron oxide the proposed mechanism involves an isolated Fe site in an open, polymeric phase.<sup>45</sup> Using time-resolved observations of OER intermediates on  $\text{Co}_3\text{O}_4$ , Zhang et al. found that a bimetallic mechanism is significantly faster than the monometallic active site in  $\text{Co}_3\text{O}_4$ .<sup>57</sup> By extension, we propose that a similar effect may be apparent here: a lower-energy bimetallic mechanism in FeOOH (as exemplified by the much lower  $R_s$  and  $R_p$  values) and a higher-energy single-site mechanism with hydrous iron oxide electrodes.

Comparisons between the 100% Ni electrodes in this study and previously published works are considerably more difficult, likely because of incidental iron contamination in previous studies. For example, Lyons and Brandon characterized the impedance of a hydrous nickel oxide electrode in 1 M NaOH and determined  $R_p$  and  $R_s$  values that were several orders of magnitude smaller than those determined here,<sup>39</sup> though we note that the Tafel slope and overpotential required to reach  $10 \text{ mA cm}^{-2}$  are consistent with an Fe-contaminated electrode.<sup>26,29</sup> Likewise, Mellsop et al. also considered the impedance of NiOOH electrodes, finding a significantly smaller total impedance, but those electrodes likewise exhibited an aging behavior consistent with incidental iron contamination.<sup>37</sup> The impedance measurements they observed are more consistent with the measurements we observe for 10% Fe, which is a reasonable value for Fe impurity uptake by NiOOH films.<sup>29</sup>

**3.3. Activation Energy.** Though the vast majority of OER work focuses on catalytic activity at room temperature, significant insight into the variation in catalytic performance can be obtained by considering the effect of temperature on activity. Specifically, the apparent electrochemical activation energy ( $E_a$ ) for water oxidation can be determined using the Arrhenius relationship<sup>58,59</sup>

$$\frac{\partial \log(i_0)}{\partial \frac{1}{T}} = -\frac{E_a}{2.3R}$$

where  $i_0$  is the exchange current density,  $T$  is the temperature, and  $R$  is the universal gas constant.

Figure 7 shows a representative plot of current density versus overpotential as a function of temperature for a 100% Ni catalyst. As the temperature is increased from 0 to  $70^\circ\text{C}$ , there

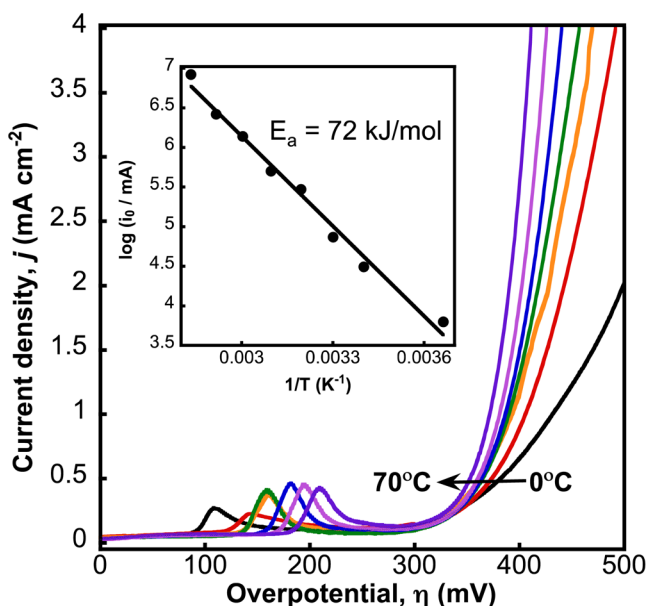


**Figure 7.** Linear sweep voltammograms as a function of temperature for a representative 100% Ni catalyst film in 1 M KOH. Inset: Arrhenius plot of the inverse temperature versus the log of the exchange current.

is a noticeable increase in the current density at lower overpotentials. An Arrhenius plot of the exchange current values obtained from the low current region (0.2 to 1 mA) versus temperature reveals linear dependence on temperature. From the slope of the Arrhenius plot, the apparent electrochemical activation energy ( $E_a$ ) can be extracted.

In Figure 8 we present activation energy as a function of composition, with the shape of the plot qualitatively consistent with that shown in Figure 2. The 100% Ni catalysts exhibited an average  $E_a$  of  $76 \pm 5 \text{ kJ mol}^{-1}$ , which is roughly  $50 \text{ kJ mol}^{-1}$  greater than the 25 and 35% Fe compositions. This significant decrease in  $E_a$  is again consistent with a model proposed by

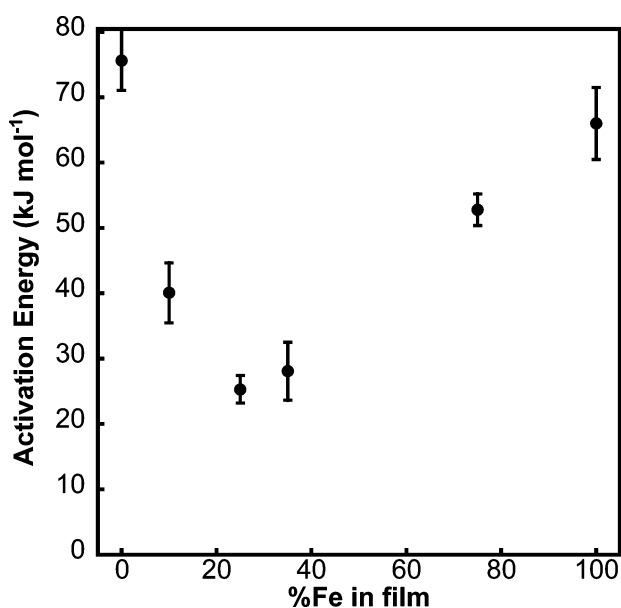


**Figure 8.** Apparent electrochemical activation energy as a function of catalyst composition.

Friebe et al.<sup>30</sup> for a decrease in the binding energy OER intermediates on Fe-doped Ni. Furthermore, in their model, these authors suggest that OER intermediates bind too strongly on pure FeOOH sites, which is reflected in the measured  $E_a$  of  $66 \pm 5 \text{ kJ mol}^{-1}$  in this study. The increased activation energies at 10 and 75% Fe are likely related to the presence of largely inactive regions of NiOOH and FeOOH within the films. We note that the shape of data in Figure 8 is qualitatively similar to the overpotential data presented in Figure 2, suggesting a direct relationship between OER activity and activation energy.

The  $E_a$  values we experimentally determined are in good agreement with the literature (Table S9). Previous studies<sup>60,61</sup> on hematite ( $\alpha\text{-Fe}_2\text{O}_3$ ) photoelectrochemically determined activation energies for water oxidation of  $43\text{--}66 \text{ kJ mol}^{-1}$ , which aligns with our value of  $66 \pm 5 \text{ kJ mol}^{-1}$  for FeOOH. For NiOOH, there is a greater disagreement between the published values<sup>62,63</sup> ( $54\text{--}63 \text{ kJ mol}^{-1}$ ) and our value ( $76 \pm 5 \text{ kJ mol}^{-1}$ ); however, those values are likely inaccurate because of iron contamination, suggesting that a better comparison may be with our 10% Fe catalyst. In this case, the measured value of  $40 \pm 5 \text{ kJ mol}^{-1}$  is more similar to the literature values. Interestingly, the  $E_a$  values for the most active catalyst compositions (ca.  $25 \text{ kJ mol}^{-1}$ ) approaches the reported values<sup>64,65</sup> for  $\text{IrO}_2$  ( $15\text{--}16 \text{ kJ mol}^{-1}$ ), which is generally considered to be one of the best OER catalysts in terms of both activity and stability.

#### 4. CONCLUSIONS

Developing a complete picture of a working OER catalyst is complicated by the many kinetic, energetic, and structural considerations in any catalyst. In this study, we utilized a combination of electrochemical impedance and activation energy measurements to gain insight into the energetics of  $\text{Fe}_x\text{Ni}_{1-x}\text{OOH}$  catalysts. Our results show that as Fe is incorporated in a NiOOH lattice, the Faradaic resistances associated with the OER decrease and charge relaxation becomes more favorable. Furthermore, our impedance results show that the formation of charged surface intermediates is the dominant process in the OER catalysis of these films. We also show from the impedance and activation energy measurements that while isolated Fe sites in NiOOH lattices have similar energetics regardless of film composition, the overall OER activity is also controlled by structural considerations. The accessible surface area and presence of inactive phases such as NiOOH or FeOOH play significant roles in controlling the observed OER current.

Finally, we also considered monometallic iron or nickel (oxy)hydroxide surfaces. In these catalysts, in situ impedance and activation energy measurements suggest that OER intermediates are poorly stabilized, leading to poor catalytic activity. The apparent activation energy for water oxidation on NiOOH is roughly  $50 \text{ kJ mol}^{-1}$  higher than on a  $\text{Fe}_{0.35}\text{Ni}_{0.65}\text{OOH}$  surface, and the overall Faradaic resistance is nearly 2 orders of magnitude higher. On a pure FeOOH surface, the overall Faradaic resistance is significantly lower than on pure NiOOH; however, the charge relaxation related to the formation of OER intermediates is quite poor. We also measured an activation energy of  $66 \pm 5 \text{ kJ mol}^{-1}$  on FeOOH, which is significantly higher than the activation energies of the most active catalysts.



## ■ ASSOCIATED CONTENT

## ■ Supporting Information

The Supporting Information is available free of charge on the ACS Publications website at DOI: 10.1021/acs.jpcc.5b05861.

Roughness factors for catalyst compositions. Tafel slope and overpotential change with time. Representative Nyquist, phase, and Bode plots for all compositions. Optimal impedance fit parameters. Reported activation energies for select OER catalysts. (PDF)

## ■ AUTHOR INFORMATION

## Corresponding Authors

\*E-mail: jrswierk@gmail.com.

\*E-mail: tdtillery@berkeley.edu.

## Notes

The authors declare no competing financial interest.

## ■ ACKNOWLEDGMENTS

This material is based upon work performed by the Joint Center for Artificial Photosynthesis, a DOE Energy Innovation Hub, supported through the Office of Science of the U.S. Department of Energy under award no. DE-SC0004993. We thank Nella Vargas-Barbosa (Pennsylvania State University) for helpful discussions during the preparation of this manuscript.

## ■ REFERENCES

- (1) Miller, E. L.; Peterson, D.; Randolph, K.; Ainscough, C. Critical Metrics and Fundamental Materials Challenges for Renewable Hydrogen Production Technologies. *MRS Online Proc. Libr.* **2014**, 1669, mrs14-1669-d01-02.
- (2) Direct Federal Financial Interventions and Subsidies in Energy in Fiscal Year 2013; U.S. Energy Information Administration: Washington, DC, 2015.
- (3) Swierk, J. R.; Mallouk, T. E. Design and Development of Photoanodes for Water-Splitting Dye-Sensitized Photoelectrochemical Cells. *Chem. Soc. Rev.* **2013**, 42, 2357–2387.
- (4) Harriman, A.; Pickering, I. J.; Thomas, J. M.; Christensen, P. A. Metal Oxides as Heterogeneous Catalysts for Oxygen Evolution Under Photochemical Conditions. *J. Chem. Soc., Faraday Trans. 1* **1988**, 84, 2795.
- (5) Nahor, G. S.; Hapiot, P.; Neta, P.; Harriman, A. Changes in the Redox State of Iridium Oxide Clusters and Their Relation to Catalytic Water Oxidation: Radiolytic and Electrochemical Studies. *J. Phys. Chem.* **1991**, 95, 616–621.
- (6) Trasatti, S.; Buzzanca, G. Ruthenium Dioxide: a New Interesting Electrode Material. Solid State Structure and Electrochemical Behaviour. *J. Electroanal. Chem. Interfacial Electrochem.* **1971**, 29, A1–A5.
- (7) Alves, V. A.; da Silva, L. A.; Boodts, J. F. C.; Trasatti, S. Kinetics and Mechanism of Oxygen Evolution on IrO<sub>2</sub>-Based Electrodes Containing Ti and Ce Acidic Solutions. *Electrochim. Acta* **1994**, 39, 1585–1589.
- (8) Carugati, A.; Lodi, G.; Trasatti, S. Fractional Reaction Orders in Oxygen Evolution From Acidic Solutions at Ruthenium Oxide Anodes. *Mater. Chem.* **1981**, 6, 255–266.
- (9) Bockris, J.; Huq, A. The Mechanism of the Electrolytic Evolution of Oxygen on Platinum. *Proc. R. Soc. London, Ser. A* **1956**, 237, 277–296.
- (10) Damjanovic, A.; Dey, A.; Bockris, J. O. Electrode Kinetics of Oxygen Evolution and Dissolution on Rh, Ir, and Pt-Rh Alloy Electrodes. *J. Electrochem. Soc.* **1966**, 113, 739.
- (11) Miles, M. H.; Klaus, E. A.; Gunn, B. P.; Locker, J. R.; Serafin, W. E.; Srinivasan, S. The Oxygen Evolution Reaction on Platinum, Iridium, Ruthenium and Their Alloys at 80°C in Acid Solutions. *Electrochim. Acta* **1978**, 23, 521–526.
- (12) Du, P.; Eisenberg, R. Catalysts Made of Earth-Abundant Elements (Co, Ni, Fe) for Water Splitting: Recent Progress and Future Challenges. *Energy Environ. Sci.* **2012**, 5, 6012–6021.
- (13) Corrigan, D. A. The Catalysis of the Oxygen Evolution Reaction by Iron Impurities in Thin Film Nickel Oxide Electrodes. *J. Electrochem. Soc.* **1987**, 134, 377.
- (14) Potvin, E.; Brossard, L. Electrocatalytic Activity of Ni-Fe Anodes for Alkaline Water Electrolysis. *Mater. Chem. Phys.* **1992**, 31, 311–318.
- (15) Singh, R.; Pandey, J.; Anitha, K. Preparation of Electrodeposited Thin Films of Nickel-Iron Alloys on Mild Steel for Alkaline Water Electrolysis. Part I: Studies on Oxygen Evolution. *Int. J. Hydrogen Energy* **1993**, 18, 467–473.
- (16) Miller, E. L.; Rocheleau, R. E. Electrochemical Behavior of Reactively Sputtered Iron-Doped Nickel Oxide. *J. Electrochem. Soc.* **1997**, 144, 3072.
- (17) Hu, C.-C.; Wu, Y.-R. Bipolar Performance of the Electroplated Iron–Nickel Deposits for Water Electrolysis. *Mater. Chem. Phys.* **2003**, 82, 588–596.
- (18) Louie, M. W.; Bell, A. T. An Investigation of Thin-Film Ni-Fe Oxide Catalysts for the Electrochemical Evolution of Oxygen. *J. Am. Chem. Soc.* **2013**, 135, 12329–12337.
- (19) Smith, R. D. L.; Prévot, M. S.; Fagan, R. D.; Zhang, Z.; Sedach, P. A.; Siu, M. K. J.; Trudel, S.; Berlinguette, C. P. Photochemical Route for Accessing Amorphous Metal Oxide Materials for Water Oxidation Catalysis. *Science* **2013**, 340, 60–63.
- (20) Fominykh, K.; Chernev, P.; Zaharieva, I.; Sicklinger, J. Iron-Doped Nickel Oxide Nanocrystals as Highly Efficient Electrocatalysts for Alkaline Water Splitting. *ACS Nano* **2015**, 9, 5180–5188.
- (21) Hunter, B. M.; Blakemore, J. D.; Deimund, M.; Gray, H. B.; Winkler, J. R.; Müller, A. M. Highly Active Mixed-Metal Nanosheet Water Oxidation Catalysts Made by Pulsed-Laser Ablation in Liquids. *J. Am. Chem. Soc.* **2014**, 136, 13118–13121.
- (22) Huang, J.-Z.; Xu, Z.; Li, H.-L.; Kang, G.-H.; Wang, W.-J. Electrochemical Studies of Iron-doped Nickel Oxide Electrode for Oxygen Evolution Reaction. *J. Electrochem.* **2006**, 12, 154–158.
- (23) Li, X.; Walsh, F. C.; Pletcher, D. Nickel Based Electrocatalysts for Oxygen Evolution in High Current Density, Alkaline Water Electrolysers. *Phys. Chem. Chem. Phys.* **2011**, 13, 1162–1167.
- (24) Landon, J.; Demeter, E.; İnöglü, N.; Keturakis, C.; Wachs, I. E.; vasić, R.; Frenkel, A. I.; Kitchin, J. R. Spectroscopic Characterization of Mixed Fe–Ni Oxide Electrocatalysts for the Oxygen Evolution Reaction in Alkaline Electrolytes. *ACS Catal.* **2012**, 2, 1793–1801.
- (25) Trotochaud, L.; Ranney, J. K.; Williams, K. N.; Boettcher, S. W. Solution-Cast Metal Oxide Thin Film Electrocatalysts for Oxygen Evolution. *J. Am. Chem. Soc.* **2012**, 134, 17253–17261.
- (26) Trotochaud, L.; Young, S. L.; Ranney, J. K.; Boettcher, S. W. Nickel-Iron Oxyhydroxide Oxygen-Evolution Electrocatalysts: the Role of Intentional and Incidental Iron Incorporation. *J. Am. Chem. Soc.* **2014**, 136, 6744–6753.
- (27) Oliva, P.; Leonardi, J.; Laurent, J. F.; Delmas, C.; Braconnier, J. J.; Figlarz, M.; Fievet, F.; de Guibert, A. Review of the Structure and the Electrochemistry of Nickel Hydroxides and Oxy-Hydroxides. *J. Power Sources* **1982**, 8, 229–255.
- (28) Desilvestro, J.; Corrigan, D. A.; Weaver, M. J. Characterization of Redox States of Nickel Hydroxide Film Electrodes by in Situ Surface Raman Spectroscopy. *J. Electrochem. Soc.* **1988**, 135, 885.
- (29) Klaus, S.; Cai, Y.; Louie, M. W.; Trotochaud, L.; Bell, A. T. Effects of Fe Electrolyte Impurities on Ni(OH)<sub>2</sub>/NiOOH Structure and Oxygen Evolution Activity. *J. Phys. Chem. C* **2015**, 119, 7243–7254.
- (30) Friebe, D.; Louie, M. W.; Bajdich, M.; Sanwald, K. E.; Cai, Y.; Wise, A. M.; Cheng, M.-J.; Sokaras, D.; Weng, T.-C.; Alonso-Mori, R.; et al. Identification of Highly Active Fe Sites in (Ni,Fe)OOH for Electrocatalytic Water Splitting. *J. Am. Chem. Soc.* **2015**, 137, 1305–1313.
- (31) Rondinini, S.; Longhi, P.; Mussini, P. R.; Mussini, T. Mercury(II) Oxide and Silver(I) Oxide Electrodes in Aqueous Solutions. *Pure Appl. Chem.* **1994**, 66, 641–647.

- (32) Wehrens-Dijksma, M.; Notten, P. Electrochemical Quartz Microbalance Characterization of Ni(OH)<sub>2</sub>-Based Thin Film Electrodes. *Electrochim. Acta* **2006**, *51*, 3609–3621.
- (33) McCrory, C. C. L.; Jung, S.; Peters, J. C.; Jaramillo, T. F. Benchmarking Heterogeneous Electrocatalysts for the Oxygen Evolution Reaction. *J. Am. Chem. Soc.* **2013**, *135*, 16977–16987.
- (34) Doyle, R. L.; Godwin, I. J.; Brandon, M. P.; Lyons, M. E. G. Redox and Electrochemical Water Splitting Catalytic Properties of Hydrated Metal Oxide Modified Electrodes. *Phys. Chem. Chem. Phys.* **2013**, *15*, 13737.
- (35) Burke, M. S.; Kast, M. G.; Trotochaud, L.; Smith, A. M.; Boettcher, S. W. Cobalt–Iron (Oxy)Hydroxide Oxygen Evolution Electrocatalysts: the Role of Structure and Composition on Activity, Stability, and Mechanism. *J. Am. Chem. Soc.* **2015**, *137*, 3638–3648.
- (36) Merrill, M. D.; Dougherty, R. C. Metal Oxide Catalysts for the Evolution of O<sub>2</sub> From H<sub>2</sub>O. *J. Phys. Chem. C* **2008**, *112*, 3655–3666.
- (37) Mellsop, S. R.; Gardiner, A.; Johannessen, B.; Marshall, A. T. Structure and Transformation of Oxy-Hydroxide Films on Ni Anodes Below and Above the Oxygen Evolution Potential in Alkaline Electrolytes. *Electrochim. Acta* **2015**, *168*, 356–364.
- (38) Lyons, M.; Brandon, M. P. The Significance of Electrochemical Impedance Spectra Recorded During Active Oxygen Evolution for Oxide Covered Ni, Co and Fe Electrodes in Alkaline Solution. *J. Electroanal. Chem.* **2009**, *631*, 62–70.
- (39) Lyons, M. E. G.; Brandon, M. P. The Oxygen Evolution Reaction on Passive Oxide Covered Transition Metal Electrodes in Aqueous Alkaline Solution. Part 1 - Nickel. *Int. J. Electrochem. Sci.* **2008**, *3*, 1386–1424.
- (40) Begum, S.; Muralidharan, V.; Ahmedbasha, C. The Influences of Some Additives on Electrochemical Behaviour of Nickel Electrodes. *Int. J. Hydrogen Energy* **2009**, *34*, 1548–1555.
- (41) Villa, M.; Milanese, C.; Nelli, P.; Salvi, P.; Verardi, E.; Marini, A.; Zangari, G. Ni - Based Electrodes for Hydrogen and Oxygen Generation. *ESC Trans.* **2009**, *16*, 9–19.
- (42) Cappadonia, M.; Divisek, J.; Heyden von der, T.; Stimming, U. Oxygen Evolution at Nickel Anodes in Concentrated Alkaline Solution. *Electrochim. Acta* **1994**, *39*, 1559–1564.
- (43) Arulraj, I.; Trivedi, D. C. Characterization of Nickel Oxy-hydroxide Based Anodes for Alkaline Water Electrolysers. *Int. J. Hydrogen Energy* **1989**, *14*, 893–898.
- (44) Osaka, T.; Yatsuda, Y. A Study on Time-Dependence of the Oxygen Evolution Reaction on Nickel by FFT Impedance Measurement. *Electrochim. Acta* **1984**, *29*, 677–681.
- (45) Doyle, R. L.; Lyons, M. E. G. An Electrochemical Impedance Study of the Oxygen Evolution Reaction at Hydrous Iron Oxide in Base. *Phys. Chem. Chem. Phys.* **2013**, *15*, 5224–5237.
- (46) Doyle, R. L.; Lyons, M. E. G. Kinetics and Mechanistic Aspects of the Oxygen Evolution Reaction at Hydrous Iron Oxide Films in Base. *J. Electrochem. Soc.* **2013**, *160*, H142–H154.
- (47) Cahan, B. D.; Chen, C.-T. The Nature of the Passive Film on Iron. *J. Electrochem. Soc.* **1982**, *129*, 474.
- (48) Cahan, B. D.; Chen, C.-T. The Nature of the Passive Film on Iron. *J. Electrochem. Soc.* **1982**, *129*, 921.
- (49) Harrington, D. A.; Conway, B. E. Ac Impedance of Faradaic Reactions Involving Electrosorbed Intermediates—I. Kinetic Theory. *Electrochim. Acta* **1987**, *32*, 1703–1712.
- (50) Kamal, H.; Elmaghraby, E. K.; Ali, S. A.; Abdel-Hady, K. Characterization of Nickel Oxide Films Deposited at Different Substrate Temperatures Using Spray Pyrolysis. *J. Cryst. Growth* **2004**, *262*, 424–434.
- (51) Patil, U. M.; Gurav, K. V.; Fulari, V. J.; Lokhande, C. D. Characterization of Honeycomb-Like “B-Ni(OH)<sub>2</sub>” Thin Films Synthesized by Chemical Bath Deposition Method and Their Supercapacitor Application. *J. Power Sources* **2009**, *188*, 338–342.
- (52) Ueta, H.; Abe, Y.; Kato, K.; Kawamura, M.; Sasaki, K.; Itoh, H. Ni Oxyhydroxide Thin Films Prepared by Reactive Sputtering Using O<sub>2</sub>+ H<sub>2</sub>O Mixed Gas. *Jpn. J. Appl. Phys.* **2009**, *48*, 015501.
- (53) Koshel, N. D.; Malyshev, V. V. Measurement of the Resistivity of the Electrode NiOOH/Ni(OH)<sub>2</sub> Solid Phase Active Substance During the Discharge Process. *Surf. Engin. Appl. Electrochem.* **2010**, *46*, 348–351.
- (54) Dillman, P.; Neff, D. Corrosion of Ferrous Archaeological and Cultural Heritage Artefacts. In *Analytical Archaeometry: Selected Topics*; Edwards, H. G. M., Vandenabeele, P., Eds.; The Royal Society of Chemistry: Cambridge, U.K., 2012; pp 399–425.
- (55) Chen, D.; Yen, M.; Lin, P.; Groff, S.; Lampo, R.; McInerney, M.; Ryan, J. A Corrosion Sensor for Monitoring the Early-Stage Environmental Corrosion of A36 Carbon Steel. *Materials* **2014**, *7*, 5746–5760.
- (56) Shoar Abouzari, M. R.; Berkemeier, F.; Schmitz, G.; Wilmer, D. On the Physical Interpretation of Constant Phase Elements. *Solid State Ionics* **2009**, *180*, 922–927.
- (57) Zhang, M.; de Respinis, M.; Frei, H. Time-Resolved Observations of Water Oxidation Intermediates on a Cobalt Oxide Nanoparticle Catalyst. *Nat. Chem.* **2014**, *6*, 362–367.
- (58) Yoo, S. J.; Sung, Y.-E. Design of Palladium-Based Alloy Electrocatalysts for Hydrogen Oxidation Reaction in Fuel Cells. In *Fuel Cell Science: Theory, Fundamentals, and Biocatalysis*; Wieckowski, A., Nørskov, J. K., Eds.; John Wiley and Sons: Hoboken, NJ, 2010; pp 111–146.
- (59) Wendt, H.; Kreysa, G. *Electrochemical Engineering: Science and Technology in Chemical and Other Industries*; Springer-Verlag: Heidelberg, Germany, 1999.
- (60) Glasscock, J. A.; Barnes, P. R. F.; Ian C Plumb, A.; Savvides, N. Enhancement of Photoelectrochemical Hydrogen Production From Hematite Thin Films by the Introduction of Ti and Si. *J. Phys. Chem. C* **2007**, *111*, 16477–16488.
- (61) Cowan, A. J.; Barnett, C. J.; Pendlebury, S. R.; Barroso, M.; Sivula, K.; Grätzel, M.; Durrant, J. R.; Klug, D. R. Activation Energies for the Rate-Limiting Step in Water Photooxidation by Nanostructured A-Fe<sub>2</sub>O<sub>3</sub> and TiO<sub>2</sub>. *J. Am. Chem. Soc.* **2011**, *133*, 10134–10140.
- (62) Jasem, S. M.; Tseung, A. C. C. A Potentiostatic Pulse Study of Oxygen Evolution on Teflon-Bonded Nickel-Cobalt Oxide Electrodes. *J. Electrochem. Soc.* **1979**, *126*, 1353.
- (63) Miles, M. H.; Kissel, G.; Lu, P. W. T.; Srinivasan, S. Effect of Temperature on Electrode Kinetic Parameters for Hydrogen and Oxygen Evolution Reactions on Nickel Electrodes in Alkaline Solutions. *J. Electrochem. Soc.* **1976**, *123*, 332.
- (64) Da Silva, L. M.; Franco, D. V.; De Faria, L. A.; Boodts, J. Surface, Kinetics and Electrocatalytic Properties of Ti/(IrO<sub>2</sub> + Ta<sub>2</sub>O<sub>5</sub>) Electrodes, Prepared Using Controlled Cooling Rate, for Ozone Production. *Electrochim. Acta* **2004**, *49*, 3977–3988.
- (65) Vargas-Barbosa, N. M. Ph.D. Dissertation. *Insights Into Electrochemical and Photoelectrochemical Water-Splitting*; The Pennsylvania State University: State College, PA, 2015.